Performance design of hypervelocity shock tube facilities

Diana Luís
dianazfluis@tecnico.ulisboa.pt

Instituto Superior Técnico, Universidade de Lisboa, Portugal

September 2018

Abstract

A new kinetic shock tube is being commissioned at Instituto Superior Técnico under funding from the European Space Agency. Its main goal is to support planetary exploration missions, by studying high-speed radiative and chemical processes kinetics relevant to planetary entries. This thesis focuses on the performance estimates made for ESTHER shock tube in both single and double stage configuration. The single stage configuration is expected to reach 8 km/s, satisfying the requirements for most Mars, Titan and LEO entries. For higher performance, using a double stage configuration, ESTHER is expected to reach up to 14.5 km/s, simulating Earth return missions and Venus entries. A drawback of the double-stage configuration is that it makes slower velocities difficult to achieve, and Mars and Titan entries have to be reproduced resorting to a few performance tweaks. More recently, there has been renewed interest in exploring Gas Giants. The atmosphere for these planets is mainly composed of molecular hydrogen with ten to twenty percent of helium and some trace elements. Although their small molecular weight means that the gas may be more easily accelerated, simulations in ground facilities are nevertheless difficult to achieve, due to high entry velocities imposed by their respective mass. Velocities up to 18.4 km/s are the fastest that can be expected to be reached by the ESTHER facility, hence, alternatives such as changing the helium and neon diluent fraction have been considered. These two changes increase the post-shock temperature, allowing important flight condition phenomena to be reproduced. Combining the high velocities obtainable with the short test times available for the experiments, an accurate trigger system is also essential for the appropriate operation of the facility. The devised ESTHER streak camera trigger system includes four sensors, an FPGA rapid development board, a FMC fast ADC converter and a signal conditioning system. These are discussed in detail in this work.

Keywords: hypervelocity, shock tube, performance, planetary entry, gas giants entry, trigger system

1. Introduction

Planetary exploration missions of Solar System atmospheric bodies has been carried out for more than 50 years. Despite the accumulated legacy, the planning for such missions remains one of the more considerable challenges for Space science. This is due -among other things- to the severe aerothermodynamic environment that occurs during the atmospheric entry phase for those spacecrafts, which occurs at extreme velocities which may easily exceed 10km/s

A summary of the planetary mission entry vehicles that reached velocities above 6 km/s is presented in table 1. As most of these missions had as primary objective the study of the atmosphere of the respective planet, the ability to provide simulations over planetary entry vehicles is essential. As performing flight experiments is extremely costly, the flow environment must be simulated using CFD codes and must be validated against ground facilities testing. Test facilities to simulate planetary entry generally either choose to simulate a scaled version of the real flight condition for a very short period of time or some specific phenomena of the real flight condition for a longer period of time.

Table 1: Planetary entry missions overview (based on Davies and Arcadi [1]).

Entry year	Name	Planet	Entry speed (km/s)
1965	FIRE II	Earth	11.35
1966	Apollo AS-201	Earth	7.67
1966	Apollo AS-202	Earth	8.29
1967	Apollo 4	Earth	10.73
1968	Apollo 6	Earth	9.60
1967	Venera 4	Venus	10.7
1978	Pioneer Venus	Venus	11.54
1995	Galileo	Jupiter	47.5
1997	Mars Pathfinder	Mars	7.26
2004	Genesis	Earth	10.8
2005	Huygens	Titan	6.2
2006	Stardust	Earth	12.9
2010	Hayabusa	Earth	12.04

More recently, there has been renewed interest in future Jovian planets entry probes. Jupiter, Saturn, Uranus and Neptune are the giants of the Solar System and they define the dominant characteristics of the planetary system. However, entering the atmosphere of a Gas Giant is a challenging engineering problem. Entry speeds into these planets are of the order of 20-50 km/s [2], resulting in extreme heating environments in the shock layer. Nevertheless, Galileo probe has successfully entered into Jupiter's atmosphere, in December 1995, with a velocity of 47.5 km/s [3].

Currently a new kinetic shock tube is being commissioned at Instituto Superior Técnico, Lisbon. The European Shock-Tube for High Enthalpy Research (ESTHER) is a combustion driver shock tube, where research in plasma radiation of shocked flows speed in excess of 14 km/s in air, is to be carried out in support of European planetary exploration missions. The overall aim of this thesis is to estimate the performance of the ESTHER shock tube in both single and double diaphragm configurations, using the STAGG code for different planetary atmospheres. Due to the very small test times expected, an accurate trigger system is required. Thereafter, the trigger system for the ESTHER shock tube is analysed and implemented into a representative signal.

2. Hypervelocity facilities outlook

Low-pressure, high speed nonequilibrium flows may be accurately simulated using shock tubes, shock tunnels or expansion tubes.Shock tubes have the indisputable advantage of generating the faithful post-shock conditions of planetary entries. Shock tube experiments generally monitor radiative emission/absorption to infer the properties of the shocked flow. However, as reported by Mirels [4], due to low density effects, the separation between the moving shock wave and the contact surface travelling behind significantly decreases with pressure, which makes it difficult to establish flows over test models.

Shock tunnels make use of the shock tube capability of compressing and heating the test gas, but a nozzle is added at the end of the shock tube. At the exit of the divergent part of the nozzle, the flow becomes hypersonic at low temperature. Thus, to simulate real flight conditions by generating hypersonic flows around bodies, shock tunnels may represent an appropriate choice [5]. However, both reflected and non-reflected shock tunnels are limited in the stagnation enthalpy that can be simulated due to the energy added to the flow across a shock wave. This is because at very high shock speeds, the flow exists as a highly dissociated plasma, which is useful to study plasma and blunt body heat transfer behind shock waves but not for aerodynamic testing. Such facilities are generally limited to Earth orbit velocities and below [6].

The expansion tube has the configuration of a conventional shock tube with addition of an expansion section attached at the downstream end of the driver tube, containing an acceleration gas [7]. After initial shock processing of the test gas in the shock tube, an unsteady expansion fan adds more energy to the final test flow, therefore the kinetic energy of the gas is increased while the temperature of the gas remains relatively low [8]. This type of facility is to be used to generate very high Reynolds number flows since the flow is never stagnated [8], which reduces dissociation and ionization [9]. However, this has the disadvantage of having much shorter test times and developing large boundary layers in the resulting test flow [9].

Another type of ground testing facilities used to study hypersonic phenomena are generally relatively low velocity and long duration, such as arc-jets, plasma torches and plasma wind tunnels. These are high enthalpy test facilities which have test times long enough for the test model to reach temperatures at which hot-wall and ablation tests can be performed. However, while they can recreate flow stagnation enthalpy, they cannot recreate the velocity or the other upstream properties of a real entry flow field. Tab. 2 summarizes the facilities capable of reaching superorbital velocities. Here, these velocities are arbitrarily considered as capable of exceeding 10 km/s.

Table 2: Superorbital flow facilities (based on Reynier [10]).

Facility	Driver technology	Stage	Perf (km/s)
EAST	Arc driven	single	46
X2	Free piston	double	10
X3	Free piston	double	10
LENS XX	Electrically heated	double	12
HVST	Free piston	double	15
ADST	Arc driven		14
ESTHER	Combustion	double	14
T6 Stalker	Free piston	double	18

3. Shock tube theory

In its simplest configuration, a shock tube consists of two different pressure sections separated by a diaphragm. However, this simple shock tube cannot generate shocks with high Mach numbers. This may be overcome adding a acceleration tube using a double diaphragm configuration.

A summary of the underlying theory of different configuration shock tubes is presented and non-ideal effects such as wall boundary layers, blast wave formation and diaphragm rupture dynamics are presented. Relevant equations are found in the thesis document.

3.1. Basic principles of ideal shock tubes

Single diaphragm, constant area: This is the simplest shock tube configuration.After diaphragm rupture, the gas in the driver section expands towards the working section, causing a normal shock wave. The shock wave propagates to the right with velocity u_s, increases the pressure of the gas behind it (region 2) and induces a mass motion with velocity u_2. The test and driver gases are separated by a contact surface, which also moves at velocity u_2 and pressure p_2. Across this contact surface, $p_3 = p_2$ and $u_3 = u_2$, but the entropy changes discontinuously. Simultaneously, expansion waves move into the high pressure section, continuously decreasing the pressure in region 4 to a lower pressure value, p_3 behind. Fig. 1 schematically shows the flowfield after diaphragm removal.

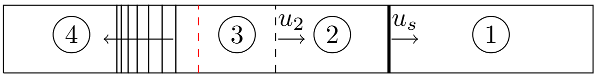

Figure 1: Flow diaphragm of a constant area ratio shock tube [not to scale].

The normal shock wave velocity is given in terms of pressure ratio, p_2/p_1, by

$$u_s = a_1\sqrt{\frac{\gamma_1+1}{2\gamma_1}\left(\frac{p_2}{p_1}-1\right)+1}. \tag{1}$$

Initial conditions of the driver and driven gases, as well as p_4/p_1 ratio determine the strengths of the incident shock and expansion waves onset after the diaphragm rupture. This ratio is given by the so-called shock-tube equation:

$$\frac{p_4}{p_1} = \frac{p_2}{p_1}\left\{1-\frac{(\gamma_4-1)\left(\frac{a_1}{a_4}\right)\left(\frac{p_2}{p_1}-1\right)}{\sqrt{2\gamma_1\left[2\gamma_1+(\gamma_1+1)\left(\frac{p_2}{p_1}-1\right)\right]}}\right\}^{-\frac{2\gamma_4}{\gamma_4-1}} \tag{2}$$

For a given diaphragm pressure ratio p_4/p_1, the incident shock strength p_2/p_1 will be stronger as a_1/a_4 is smaller. As $a = \sqrt{\gamma RT} = \sqrt{\gamma(\mathcal{R}/\mathcal{M})T}$, being γ the specific heats ratio, $\mathcal{R}$ the perfect gas constant and $\mathcal{M}$ the molar mass of the gas, the speed of sound is faster in a hot light gas than in a cold heavy gas. Thus, to maximize the incident shock strength for a given p_4/p_1, the driver gas should be a low molecular weight gas at high temperature (hence high a_4) and the test gas should be a high molecular weight gas at low temperature (hence low a_1).

Single diaphragm, variable area: The schematic diagram for this configuration is presented in Fig. 2.

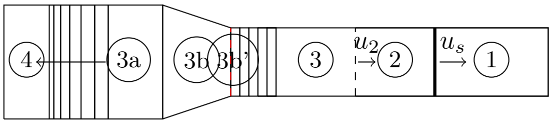

Figure 2: Flow diagram of shock tube with convergent geometry [not to scale].

For the following analysis, except across the shock itself, isentropic processes and ideal gas behaviour are assumed.

At diaphragm removal, energy is extracted from the driver gas through an unsteady expansion from state 4 to state 3a. Based on Alpher and White [11] and considering the general case of a convergent-divergent diaphragm section, the pressure ratio p_4/p_1 may be expanded as

$$\frac{p_4}{p_1} = \frac{p_4}{p_{3a}}\frac{p_{3a}}{p_{3b'}}\frac{p_{3b'}}{p_{3b}}\frac{p_{3b}}{p_3}\frac{p_3}{p_2}\frac{p_2}{p_1} \tag{3}$$

where p_4/p_{3a} is the ratio required to accelerate the driver gas through an unsteady expansion from rest to the Mach number M_{3a}; $p_{3a}/p_{3b'}$ is the ratio required to bring the driver gas by a steady expansion from M_{3a} to $M_{3b'}$; $p_{3b'}/p_{3b}$ is the ratio required to bring the gas by a steady expansion from $M_{3b'}$ to M_{3b} through an area ratio $A_{3b'}/A_{3b}$; and p_{3b}/p_3 is the ratio needed from an unsteady expansion from M_{3b} to M_3. At the contact surface, $p_3 = p_2$.

Applying the non-steady expansion wave relations through regions $4-3a$ and $3b-3$, the steady expansion wave relations through the supersonic nozzle (region $3a-3b$) and the pressure boundary condition, $p_3 = p_2$, equation 3 yield

$$\frac{p_4}{p_1} = \frac{1}{g}\frac{p_2}{p_1}\left[1-\frac{u_2}{a_1}\frac{a_1}{a_4}\frac{\gamma_4+1}{2}g^{-\frac{\gamma_4-1}{2\gamma_4}}\right]^{-\frac{2\gamma_4}{\gamma_4-1}} \tag{4}$$

where the quantity g is the equivalence factor defined as [11]

$$g = \left\{\left[\frac{2+(\gamma_4-1)M_{3a}^2}{2+(\gamma_4-1)M_{3b}^2}\right]^{\frac{1}{2}}\left[\frac{2+(\gamma_4-1)M_{3b}}{2+(\gamma_4-1)M_{3a}}\right]\right\}^{\frac{2\gamma_4}{\gamma_4-1}}. \tag{5}$$

Double diaphragm, variable area: A simple shock tube cannot generate shocks with extremely high Mach numbers and the corresponding attainable post-shock temperature is low. To increase the shock Mach number, the ratio of sound speeds in the driver and working gases must be increased. This may be achieved by using different gases or heating the driver gas. Another alternative is to use cross-sections area reduction at the diaphragm. This causes a steady expansion wave in the driver gas in the subsonic region of the flow which is thermally more efficient than an unsteady expansion.

When the first diaphragm ruptures, a primary shock wave with velocity u_{s7} is produced, processing it to a contact surface with velocity u_6 and creating expansion waves. Once this primary shock wave reaches the second diaphragm, it is reflected and the pressure and temperature increase. At diaphragm opening, a main shock wave is produced, with a velocity u_{s1} greater than the velocity of the primary shock wave. Based on the initial conditions, properties in region 11 (driver section), region 7 (intermediate section) and region 1 (working section), before the diaphragm removal, are known. A schematic representation for the different zones after both diaphragmss burst is presented in Fig. 3.

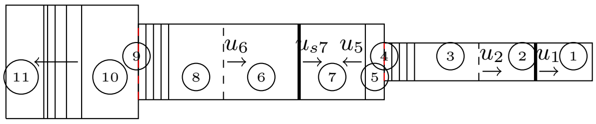

Figure 3: Flow diagram of a double shock tube with two cross-section area reductions [not to scale].

3.2. Disturbance effects

In an ideal shock tube, the shock wave propagates with velocity u_s and the contact surface with velocity u_2, both at constant pace. However, in an actual shock tube, the presence of a wall boundary layer alters the velocity for the main shock wave and the main contact surface. This boundary layer between shock and contact surface removes mass from this region, causing the shock to decelerate and the contact surface to accelerate. The flow becomes non-uniform and the separation distance decreases below the ideal value, reducing effective test time.

Wall boundary layer Boundary layer effects have been studied by many authors. Trimpi and Cohen [12], Mirels [13], Dem'yanov [14] and Spence and Woods [15] presented wall boundary layer theories that were primarily concerned with the unsteady motion of the shock. Roshko [16], Hooker [17], Mirels [4, 18] and Ackroyd [19] theories sought to predict only the duration of the hot flow, while satisfying the condition of mass continuity between the shock and the contact surface. According to Mirels [4], in a conventional shock tube, the separation between the contact surface and the shock wave increases as the distance until the diaphragm increases. However, in a low pressure shock tube, Duff [20] observed that at a certain point, the separation reaches a maximum value and that, after the limiting value, the contact surface and the shock both move with equal and constant velocity.

Wall drag effects on shock velocity As the boundary layer grows, the speed of the shock wave is reduced through drag effects. Milne [21] developed a simplified theory to estimate these effects through the addition of a source term to the ideal case. For a circular cross-section tube of working diameter d_1, the momentum source term per unit length of tube is given by

$$S_w = \frac{4\int_0^{d_1} \tau_w dz}{d_1^2} = \frac{4\tau_w}{d_1}, \tag{6}$$

where d_1 is the diameter of the working section and τ_w the wall friction, that is expressed as function of the coefficient of friction, C_f, and the ideal speed and density of the shock, respectively, u_s and ρ_s,

$$\tau_w = C_f \frac{\rho_s u_s^2}{2}. \tag{7}$$

The coefficient of friction is parametrized in terms of the Reynolds number, Re, by

$$C_f = \begin{cases} 64/\text{Re} & \text{if Re} < 1200 \\ 0.316/\text{Re}^{\frac{1}{4}} & \text{if } 1200 < \text{Re} < 10^5 \\ 0.00332 + 0.221/\text{Re}^{0.237} & \text{if Re} > 10^5 \end{cases} \tag{8}$$

where $\text{Re} = (d_1/\nu)u_s$. ν corresponds to the kinematic viscosity

$$\nu = \mu \frac{\sqrt{T_s/3000}}{\rho_s} \tag{9}$$

and the viscosity μ, a function of the gas in the shock tube, is typically approximated by 10^{-4} [21].

Given these parameters, the momentum source term may be added to the velocity equation, and calculated iteratively by

$$u_{losses}(i) = u_{losses}(i-1) - \frac{S_w dx}{\rho_s} \tag{10}$$

with $u_{losses}(i-1)$ the velocity in the previous step, and dx the step length.

Blast wave formation For sufficiently long shock tubes, it is experimentally observed that the wave structure (that comprises the shock wave, contact surface and a family of expansion waves) eventually evolves into a shape resembling an air blast wave [22]. To study this, the wave interactions taking place upon the reflection of the head expansion wave at the left end wall need to be considered. Once the reflected head wave reaches the right-propagating shock, it marks the onset of the Friedlander wave form in the shock tube. The determination of the location for the onset of the wave form only requires tracking the evolution of the head wave. Note that this algorithm was developed solely for single diaphragm configurations, hence the notation for this configuration assuming unitary area ratios.

The location of the Friedlander wave is given by

$$L = L_4 + u_s t_d \tag{11}$$

where L_4 is the length of the driver section, u_s is the shock speed and t_d is the time of onset of the Friedlander wave, given by

$$t_d = \frac{2L_4 a_2}{a_4(u_2 + a_2 - u_s)} \left(\frac{p_4}{p_2}\right)^{\frac{\gamma_4+1}{4\gamma_4}} . \tag{12}$$

where, a_2 and a_4 are the sound speeds, and p_2 and p_4 the driver pressures, respectively behind the shock and initially at the driver section; γ_4 is the specific heat ratio in the driver section.

Secondary diaphragm rupture Many theories have been proposed to model the diaphragm rupture process. The ideal rupture model is usually used as a first approach and considers the secondary diaphragm to be infinitely thin and massless, to rupture instantaneously on impact by the primary shock and, therefore, to have no impact on the flow.

In reality, the diaphragm interferes with the flow during and after rupture. The two most widely used approaches are the diaphragm inertia and holding time rupture models, that take into account the finite rate opening time of the secondary diaphragm.

The inertia model was proposed by Morgan and Stalker [23] and assumes that the diaphragm breaks instantaneously once the primary shock hits it and then it stays together as an obstacle in the flow field. The reflected shock is weakened over time through interaction with expansion waves caused by diaphragm acceleration.

The holding time rupture model, proposed by Haggard [24], notes the time of arrival of the primary shock at the secondary diaphragm and, after a specific time, the diaphragm is instantaneously removed. The holding time secondary diaphragm rupture model underestimates the test gas recombination through the unsteady expansion [25]. However, it provides a simple pre-rupture flow field.

4. Performance design

Requirements for ESTHER design call for a facility beyond the current state-of-the-art with an emphasis on superorbital flow regimes. This drives the facility design optimization.

The first optimization concerns the driver to working area ratios. the shock speed gains due to area change[1] are presented in Fig. 4.

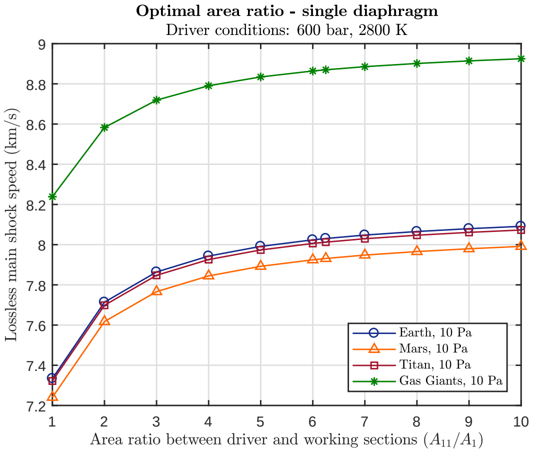

Figure 4: Effect of area ratio (single diaphragm configuration).

The shock speeds increase logarithmically with area ratio increase, up to a point where the gains become marginal An overall area ratio of 6.25:1 was chosen, as a practical upper limit as with the Convair shock tunnel [26]. The second-stage tube area (between the 6.25:1 ratios) is then optimized to yield the highest working section shock speed.

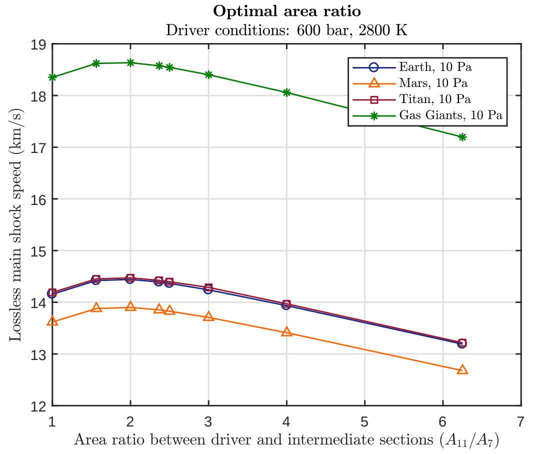

Figure 5: Effect of area ratio (double diaphragm configuration).

The optimal driver to intermediate area ratio is about 2 for the 6.25:1 overall area ratio. As the ESTHER working section tube diameter is 80 mm, the other ones should respectively be 130 mm and 200 mm for the second stage and driver sections.

Then the optimal intermediary pressure has to be estimated. Fig. 6 presents the pressure-dependednt performance [2].

Overall, improvements in speed between 30% and 45% are obtained when comparing two-stage to one-stage configurations.

---

[1] in single stage mode

[2] for both single and double stages configurations

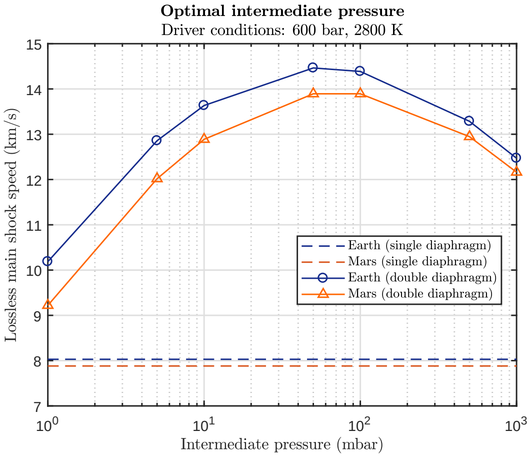

Figure 6: Effect of intermediate pressure.

4.1. Performance discussion

The performance envelope for the ESTHER shock-tube, in single and double stage configurations, has been obtained for several planetary atmospheres and is presented in Fig. 7. The single stage mode performance is not discussed in detail, since its operation range is much more narrower than the double stage one.

For Earth's atmosphere, the maximum shock speeds (including losses) vary between about 11.5 km/s and 14.5 km/s, for working pressures between 10 Pa and 100 Pa. Minimum velocities range between 5.5 and 9.5 km/s. The facility can accordingly reproduce any fast Earth entry. Venus, Mars and Titan fast entries can also be comfortably be reproduced, with minimum shock speeds between about 5 and 9km/s for CO_2–N_2 atmospheres, and maximum shock speeds between 11 and 14 km/s. Titan entry performance is nearly identical to Earth reentry performance, owing to the nigh identical test gas molecular masses.

Gas Giants entries are simulated considering a 90% H_2 and 10% He gas mixture. Since the test gas is lighter, higher speeds are reached, up to a maximum of 18.36 km/s for 10Pa ambient pressure. The lowest possible Gas Giant entry speed is Uranus entry at 22.3 km/s, therefore no direct reproduction of a Gas Giant entry is possible within the double stage configuration of ESTHER. Alternative venues for reproducing such shock speeds as recently proposed by James et al. [27], have to be considered: increasing the test gas helium composition, or helium gas substitution by neon. Although these techniques do not sensibly increase shock velocity[3], they do increase the post-shock temperature, allowing the partial reproduction of post-shock flow conditions in Gas Gaints entries.

Fig. 8 presents helium (He) and neon (Ne) molar fractions influence on post-shock variables.

When adding helium diluent to the H_2/He mixture, the shock speeds increase about only 3.8%, while the post-shock temperature more than doubles, comparing the results for 90% He to those for 10% He. In the case of addition of neon to the H_2/He mixture, as a consequence of its five times higher molecular weight compared to helium, shock layer conditions with significant levels of dissociation and ionization may be reproduced at achievable speeds. Moreover, even though the shock speed decreases slightly, the post-shock temperature increases around 42%. Thereafter, despite the low shock speeds achieved when simulating Gas Giants entries, even with helium or neon diluent, the entry frozen temperature may be recreated in ground facilities.

Regarding wall loss mechanisms, Milne's [21] model evidenced shock speed losses increasing between 30 and 50 m/s as the test gas pressure decreases, independently of the test gas compositions. Higher losses up to 200m m/s are reported for Gas Giants mixtures, with no clear pressure dependence. However the viscosity model, based on air gases, may be questionable in this specific case and must be validated.

The viscous test times were computed based on Mirels [4] and Milne's [21] theories. There was a large discrepancy between the results obtained. As Mirels' theory presents the more pessimistic results, these should be the ones considered, prior to getting actual experimental results. However, his theory was deducted for weak shock speeds, hence the theory might be applied outside its validity range. Nevertheless, considering these results as pessimistic, the test times may vary between 3.5 μs and 21.7 μs, for single diaphragm configuration, and between 1.3 μs and 30.7 μs, for double diaphragm configuration. Again, the worst estimated test times correspond to Gas Giants' atmosphere, as the test time decreases with the increase of the shock speed. Adding neon diluent into the H_2/He gas decreases the shock speed. Thereafter, this addition is expected to increase the test time.

A final cross-check has been caried out to certify the absence of blast waves in any configuration. Tasissa et al's [22] algorithm was implemented in single stage configuration. It was predicted that blast wave formation occurs almost 800 m ahead of the diaphragm position, which is much longer than the actual shock tube length. For double stage configuration, the algorithm was applied considering the properties of the intermediate section. The intersection of the head of the expansion wave with the primary shock wave occurs after the main shock wave passes the observation window (around 150 m after the first diaphragm position). This is corrob-

---

[3] and may even decrease it in the case for neon

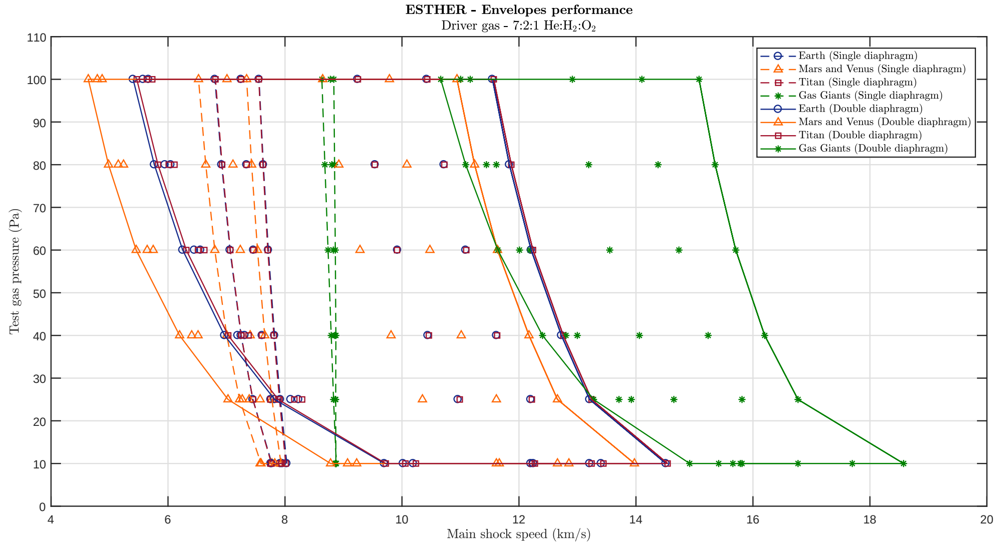

Figure 7: Envelope performance for different planetary atmospheres.

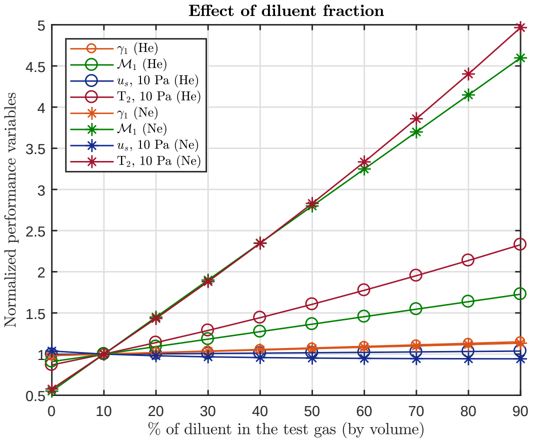

Figure 8: Effects of helium and neon diluent.

orated through the wave diagrams elaborated using the characteristics method, and presented in Fig. 9.

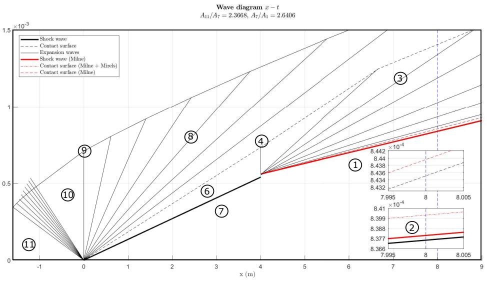

Figure 9: Wave diagram for ESTHER in double diaphragm configuration.

A final remarks may be made regarding the ESTHER performance envelope in Fig. 7: Since ESTHER is tailored for high-speed performance, it has trouble reaching low speeds. These lower speed ranges might still be desirable for flight testing, one good example being the atmospheric entry in Mars, where peak radiative heat fluxes (CO_2 IR radiation) are expected to occur at significantly lower speeds then peak convective heating, around 3 km/s [28].

Lower velocities may be achieved through two possible techniques: 1) changing the intermediate pressure to its lowest value; and 2) changing the driver gas for a heavier mixture. The first technique was considered when designing the envelope performance. As the highest working pressure is 100 Pa, the lowest intermediate pressure that may be considered is 1 mbar (100 Pa), since it should not be inferior to the working pressure. When considering the lowest driver to working pressures ratio and a non optimized intermediate pressure, the low driver to intermediate pressures ratio creates a weak primary shock wave, which will be then slowly accelerated in the working section, resulting in the slowest obtainable shock.

Focusing on the second technique, one may try to achieve shock speeds lower than the ones for a driver mixture of 7:2:1 He:H_2:O_2, by substituting the helium dilutant by nitrogen, keeping the mixture ratio. Not only the driver gas becomes heavier, but also the rotational-vibrational modes of N_2 will absorb a certain amount of combustion heat. Hence, the shock speed is expected to be lower. This second technique has not been considered in this work due to lack of time for producing an updated equilibrium gas model.

5. Trigger system

As the facility test times are expected to be very small, a high-performance, accurate trigger system is necessary. Here, the development of this trigger system and the associated pressure sensors are discussed.

5.1. Streak camera trigger proposal

The original streak camera system was being developed by IUSTI, from University of Provence. The system was composed by five piezoelectric sensors, four before and one after the camera and based on ECL fast electronics. Despite the schematic design being already finalized and some components already bought, there were a few disadvantages inherent to IUSTI project. Therefore, a new schematic design was devised, using FPGA based hardware and fast analogue to digital converter (ADC).

The new streak camera system design proposes the selection of only four sensors (three before and one after the camera), a FPGA rapid development board, a FMC fast ADC converter and a signal conditioning system, as presented in Fig. 10.

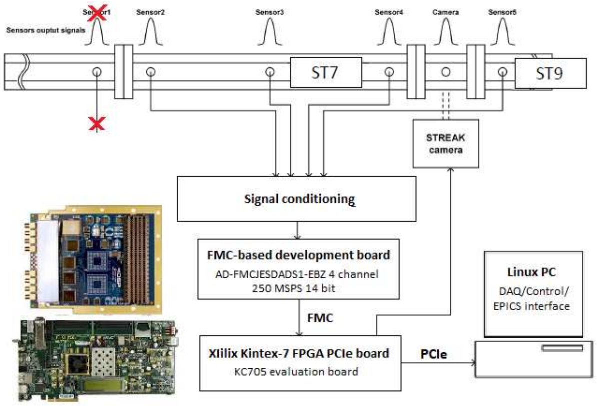

Figure 10: Streak camera system.

The KC705 evaluation board was selected, providing a hardware environment for developing and evaluating designs targeting the Kintex-7 FPGA [29].

The FMC-based development board is a high speed data acquisition that comprises four 14-bit ADC channels with sampling speeds up to 250 MS/s [30]. The firmware for this system was developed in VIVALDO based on a reference design project available from Analog Devices (FMC-176 [30]).

As the FMC-176 board only has four ADC channels, the number of sensors that can be connected is limited to four (three before and one after the camera). Two sensors before the camera position are the strict minimum to measure the delays, with the third sensor providing a cross-check of the time threshold before sending it to the camera. The sensor after the camera is used to validate and recalibrate the results, downstream of the camera. These sensors cannot be directly connected to the FMC development board, hence, a ”signal conditioning” system needs to be developed. The ”signal conditioning” system can be divided into two parts, depending on two types of available sensors that is connected to: piezoelectric (PE) sensors or integrated electronics piezoelectric (IEPE) sensors.

This system is expected to precisely detect the speed of the passing wave and generate an accurate time trigger signal for the diagnostic at a clock speed of 125 MHz.

5.2. Trigger generation

Heaviside signal A simplified model is firstly analysed to outline the FPGA algorithm, For this model, there are three input signals (corresponding to the sensors before the camera) considered to be heavisides: initially at zero, increasing immediately to one once the wave intercepts the sensor. The outputs of the sensors are modelled by the response of a Butterworth second order filter, with cutoff frequency ω_n, and simulated white noise. The results are illustrated in Fig. 11.

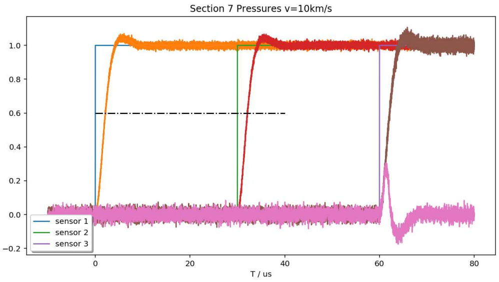

Figure 11: Simulation with a heaviside signal.

The dash-dotted line corresponds to the threshold voltage level which is arbitrarily chosen. As the rise time for the different filtered signals may be considered equal, the trigger level can be altered theoretically without influencing the time delay. Once the first signal output (orange signal) reaches that value, the system starts counting the time until the second signal output (red signal) exceeds it as well. The difference between the passage of both signals corresponds to the delay time.

For the third signal, instead of using the previous algorithm, the constant fraction zero-crossing discriminator (CFD zero-crossing) method is implemented. The advantage of this algorithm is such that the delay has a lower dependency on the amplitude of the filtered signal, compared with the threshold algorithm.

Alongside the third filtered signal (brown signal), a new signal (pink signal) is generated at FPGA level. The pink signal is a double differentiation of a moving average of the brown signal. For the CFD zero-crossing method, the instant when the pink signal crosses the zero is measured and to that value, the threshold time calculated previously is summed and multiplied by two constants: gain and offset. These allow correcting the results. The resulting time corresponds to the instant at which the front wave will pass and, therefore, the streak camera should record the values. The fourth sensor is placed after the camera to verify if the instant at which the camera recorded the values was correct. If not, it also provides data to adjust that value.

Real signal A representative signal from the X2 expansion tube (University of Queensland) was extracted from James et al. [31], so as to more accurately study and predict the behaviour of the trigger system. As the ESTHER will have at most three sensors before the streak camera, the aforementioned algorithms were only implemented on the first three signals.

The influence of the cutoff frequency of the Butterworth filter on the output signal may also be analysed. The parameter ω_n was altered between 0.0005, 0.001 and 0.002. Figure 12 presents the input and output signals obtained for $\omega_n = 0.0005$.

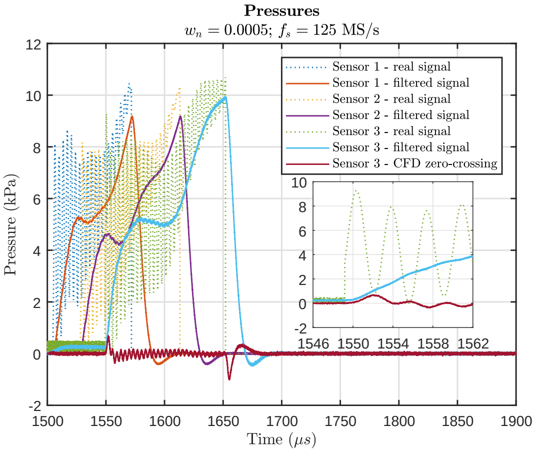

Figure 12: Filtered signal pressures.

The comparison between the different cases showed that once the cutoff frequency is decreased, there is a reduction of oscillations of the filtered signal. However, there is also an increase of the rise time for the filtered signal and further an attenuation of the maximum frequency that passes the filter, which in turn alters the value of the maximum post-shock wave pressure by almost 12% (when comparing the extreme cases analysed).

Nevertheless, for the trigger system to accurately measure the threshold time, the relevant information is the time difference between two points at the same level, hence the same pressure, from the first two consecutive sensors. The cutoff frequency must accordingly be chosen such that the signal oscillations due to noise do not intersect the threshold level more than once. Those oscillations are clearly visible for higher cutoff frequencies.

For the third signal, the cutoff frequency slightly influences the maximum post-shock wave pressure (only 3%), while the signal resulting from the CFD zero-crossing (red signal) is significantly altered. For low cutoff frequencies, the differentiated signal is critically attenuated and the zero-crossing may even not occur for the shock front wave signal (as seen in the zoom of the signal for $\omega_n = 0.0005$, in the smallest box in figure 12). When increasing the cutoff frequency, the intersection with zero occurs earlier than for an inferior frequency. This intersection instant is then corrected by the constants, for the calculation of the final time sent to the streak camera.

6. Conclusions

The primary objective of this thesis was to estimate the performance design of the new ESTHER shock tube. For different planetary atmospheres, the lossless shock speeds have been simulated, using the STAGG code. The wall drag losses were computed applying Milne's algorithm and the test times were predicted based on Mirels' work. As the ESTHER shock tube is expected to have a very small test time, an accurate trigger system was then discussed.

The initial theoretical predictions have provided the optimal area ratios which yield the optimal shock speeds, and, for a double stage shock-tube, the optimized intermediate pressure. The lowest shock speeds are achievable in turn for the lowest driver to working pressures ratio and a non optimized intermediate pressure.

Simulations for Earth, Mars and Venus, Titan and Gas Giants' gas compositions were analysed and, with the notable exception of Gas Giants, the required superorbital atmospheric entry velocities are expected to be reached, using a double diaphragm configuration.

Gas Giants simulations were also carried out using a pessimistic equilibrium gas model and a maximum shock speed of 18.4 km/s was predicted. As this speed is not enough to simulate Gas Giants entries, gas substitutions were analysed and it was concluded that both neon and helium may simulate the frozen entry temperatures.

The estimates for disturbance effects predicted wall losses to be only dependent on the working pressure, at the again notable exception of Gas Giants atmospheres which had higher wall losses; the test time by Mirels' theory to be very small and highly dependent on the shock speed; and the blast wave initiation length to be much longer than the actual length of the shock tube.

As the test times are expected to be very small, a very accurate trigger system is necessary. The system devised for ESTHER was briefly explained and the FPGA algorithm was implemented for a simplified model and then on a representative signal. The influence of the cutoff frequency on the latter was analysed and it was verified that, when decreasing the cutoff frequency, there is a reduction of oscillations of the filtered signal, an increase of the rise time and an attenuation of the maximum post-shock wave pressure. When implementing the CFD zero-crossing method, it was verified that the cutoff frequency influences slightly the maximum post-shock pressure, while the differentiated signal is critically attenuated for low cutoff frequencies.

References

[1] C. Davies and M. Arcadi, "Planetary mission entry vehicles quick reference guide. Version 3.0," Tech. Rep. NASA/SP-2006-3401, NASA Ames Research Center, January 2006.

[2] P. A. Gnoffo, "Planetary-entry gas dynamics," *Annual Review of Fluid Mechanics*, vol. 31, no. 1, pp. 459–494. `https://doi.org/10.1146/annurev.fluid.31.1.459`.

[3] A. Seiff, E. Venkatapathy, B. L. Haas, and P. Intrieri, "Galileo probe aerodynamics," in *14th AIAA Applied Aerodynamics Conference*, no. AIAA-96-2451, June 1996. `https://doi.org/10.2514/6.1996-2451`.

[4] H. Mirels, "Test time in low-pressure shock tubes," *The Physics of Fluids*, vol. 6, pp. 1201–1214, September 1963. `https://doi.org/10.1063/1.1706887`.

[5] R. Brun, "Shock tubes and shock tunnels: Design and experiments," tech. rep., Universit dAix-Marseille, September 2009.

[6] R. G. Morgan, "A review of the use of expansion tubes for creating superorbital flows," in *AIAA, Aerospace Sciences Meeting & Exhibit, 35th*, January 1997. `http://doi.org/10.2514/6.1997-279`.

[7] C. I. Morris, *Shock-induced combustion in high-speed wedge flows.* PhD thesis, Stanford University, December 2001.

[8] A. Dufrene, "High enthalpy studies of capsule heating in an expansion tunnel facility," tech. rep., CUBRC, 2012.

[9] R. Morgan, "Free-piston driven expansion tubes," *Handbook of Shock Waves*, vol. 1, pp. 603–622, 2001. `https://doi.org/10.1016/B978-012086430-0/50014-2`.

[10] P. Reynier, "Survey of high-enthalpy shock facilities in the perspective of radiation and chemical kinetics investigations," *Progress in Aerospace Sciences*, vol. 85, 2016.

[11] R. A. Alpher and D. R. White, "Flow in shock tubes with area change at the diaphragm section," *Journal of Fluid Mechanics*, vol. 3, no. 5, pp. 457–470, 1958. `https://doi.org/10.1017/S0022112058000124`.

[12] R. L. Trimpi and N. B. Cohen, "A theory for predicting the flow of real gases in shock tubes with experimental verification," Tech. Rep. NACA-TN-3375, National Advisory Committee for Aeronautics, March 1955.

[13] H. Mirels, "Attenuation in a shock tube due to unsteady-boundary-layer action," Tech. Rep. 1333, National Advisory Committee for Aeronautics, 1957.

[14] Y. A. Dem'yanov, "The influence of the boundary layer on the character of the flow of gas in a tube behind a moving shock wave," Tech. Rep. 796, R.A.E. Library Translation, 1959.

[15] D. A. Spence and B. A. Woods, "Boundary layer and combustion effects in shock tube flows," in *Proceedings XI Symposium of the Colston Research Society*, Butterworths Sci. Pub., 1959.

[16] A. Roshko, "On flow duration in lowpressure shock tubes," *The Physics of Fluids*, no. 3, 1960. `https://doi.org/10.1063/1.1706147`.

[17] W. J. Hooker, "Testing time and contact-zone phenomena in shock-tube flows," *The Physics of Fluids*, vol. 12, no. 4, 1961. `https://doi.org/10.1063/1.1706147`.

[18] H. Mirels, "Shock tube test time limitation due to turbulent wall boundary layer," *AIAA Journal*, vol. 2, no. 84, 1964.

[19] J. A. D. Ackroyd, "A study on the running times in shock tubes," tech. rep., Department of Aeronautics, Queen Mary College, 1964.

[20] R. E. Duff, "Shock tube performance at low initial pressure," *The Physics of Fluids*, vol. 2, pp. 207–216, March 1959. `https://doi.org/10.1063/1.1705910`.

[21] A. Milne, "Wall effects in a 1D shock tube." Private communication, July 2017.

[22] A. F. Tasissa, M. Hautefeuille, J. H. Fitek, and R. A. Radovitzky, "On the formation of Friedlander waves in a compressed-gas-driven shock tube," in *Proc. R. Soc. A*, vol. 472, 2016. `http://doi.org/10.1098/rspa.2015.0611`.

[23] R. G. Morgan and R. J. Stalker, "Double diaphragm free piston driven expansion tube," in *Proceedings of the 19th International Symposium on ShockWaves*, pp. 1031–1038, July 1991.

[24] K. V. Haggard, "Free-stream temperature, density and pressure measurements in an expansion tube flow," Technical Note 502-27-01-03, NASA Langley Research Center, Hampton, Va. 23665, October 1973.

[25] P. Jacobs, R. Morgan, A. Brandis, David, Buttsworth, A. Dann, M. D'Souza, T. E. D. Gildfind, R. Gollan, C. Jacobs, M. McGilvray, T. McIntyre, N. Mudford, H. Porat, D. Potter, and F. Zander, "Design, operation and testing in expansion tube facilities for superorbital re-entry," tech. rep., The University of Queensland, May 2013.

[26] A. J. Smith, "ESTHER performance estimation," Tech. Rep. CR111/11, Fluid Gravity Engineering, October 2011.

[27] C. M. James, D. E. Gildfind, R. G. Morgan, S. W. Lewis, E. J. Fahy, and T. J. McIntyre, "On the current limits of simulating gas giant entry flows in an expansion tube," in *20th AIAA International Space Planes and Hypersonic Systems and Technologies Conferences*, July 2015. `http://doi.org/10.2514/6.2015-3501`.

[28] M. Lino da Silva and J. Beck, "Contribution of CO_2 IR radiation to martian entries radiative wall fluxes," in *49th AIAA Aerospace Sciences Meeting Including the New Horizons Forum and Aerospace Exposition*, January 2011. `http://doi.org/10.2514/6.2011-135`.

[29] Xilinx, "KC705 Evaluation Board for the Kintex-7 FPGA," July 2018. Available online: `https://www.xilinx.com/support/documentation/boards_and_kits/kc705/ug810_KC705_Eval_Bd.pdf`.

[30] Analog Devices. `https://wiki.analog.com/resources/fpga/xilinx/fmc/ad-fmcjesdadc1-ebz`, accessed August 21, 2018.

[31] C. M. James, D. E. Gildfind, S. Lewis, R. G. Morgan, and F. Zander, "Implementation of a state-to-state analytical framework for the calculation of expansion tube flow properties," *Shock Waves*, vol. 28, pp. 349–377, 2018. `http://doi.org/10.1007/s00193-017-0763-3`.